Solid Freeform Fabrication 2021: Proceedings of the 32nd Annual International Solid Freeform Fabrication Symposium – An Additive Manufacturing Conference
Reviewed Paper

Linear elastic finite element calculations of short cracks initiated from the defects: effect of defect shape and size

Arun Poudel, Nima Shamsaei, Shuai Shao *

National Center for Additive Manufacturing Excellence (NCAME), Auburn University, Auburn, AL 36849, USA

Department of Mechanical Engineering, Auburn University, Auburn, AL 36849, USA

* Corresponding author: sshao@auburn.edu

Abstract

The defects present in an additively manufactured component deteriorate its mechanical, especially fatigue performance. During loading, these defects influence the stress concentration, promote the fatigue crack initiation and thus, lead to a lower fatigue performance. In this study, the effect of defect shape and size on the Mode-I stress intensity factor (K_I) of the short cracks initiating from both 2D and 3D internal defects was investigated using linear elastic finite element analysis (FEA). The shape of the defect was varied by altering the aspect ratio (width/height) from 0 to 1. Later, the dimensionless results from FEA were utilized to calculate the SIF in defects with half-span width of range 10-100 μm. As a result, the influence of defect shape on the SIF was only observed in the short crack length regimes and the measure of SIF was observed to increase with decreasing aspect ratio for a given crack length.

Keywords: Linear elastic finite element analysis, Stress intensity factor, Three-dimensional defects, Effect of defect shape

Introduction

Additive manufacturing (AM) processes are prone to induce defects in the fabricated parts [1,2]. In the machined surface condition, volumetric defects, such as lack of fusion (LoF) defects, keyholes, and gas-entrapped pores, act as stress risers, accelerate the fatigue crack initiation under cyclic loading [3], and compromises the fatigue performance of additively manufactured (AM) parts [4,5]. In the high cycle fatigue (HCF) regime, where the initiation phase of fatigue cracks occupies a major portion of the fatigue life, the detrimental effects of defects is the most significant. An order of magnitude shorter fatigue lives as compared to the wrought counterparts have routinely been witnessed for AM materials [6–9]. In the low cycle fatigue (LCF) regime, where the fatigue crack propagation is more important, the AM defects' deleterious effect is less pronounced [10][11]. In fact, the fatigue crack propagation rates in the Paris regime of AM alloys are largely comparable to their wrought counterparts [12][13]. Various defect sensitive fatigue models such as Murakami, El-Haddad, etc. have shown the potential to correlate defect sizes with fatigue strength [14–17].

There exists a research gap in understanding the effect of defect shape on the K_I which is a main driving force for the cracks to propagate. Models such as Murakami's approach correlate the projected size of the defect with the Mode-I stress intensity factor (K_I) without addressing its shape

[17], although the shape of the defect has already been observed to influence the local stress field surrounding the defect [18]. Similar observations were also made on the two-dimensional surface notch, where the shape of the notch affected the K_I of the crack originating from it [19]. Specifically, shaper notches with lower aspect ratios were shown to generate higher K_I as compared to ones with higher ratios. However, such a study for internal defects, especially in three-dimensional configurations, has been lacking.

Hence, in this study, the effect of defect shape and size on the Mode-I stress intensity factor (K_I) of crack originating from internal defects was investigated. This work mainly comprises the linear elastic finite element analysis (FEA) of internal defects in both two-dimensional (2D) and three-dimensional (3D) configurations. Later, the dimensionless results obtained from the FEA were utilized to calculate the corresponding SIF value for different size defects with half-span width of range 10-100 μm.

Methodology

In the FEA of this work, two different types of internal defect configurations were considered, namely two-dimensional (2D) and three-dimensional (3D) configurations. Variables such as a, b, and c were introduced to represent the half-span width, half-span depth, and half-span crack length (see **Fig. 1**). During the analysis, defect shape was varied by altering the aspect ratio (i.e., b/a) from pure crack (i.e., 0) to 1. The lower aspect ratio corresponds to the defects such as lack of fusion and higher ones to the spherical gas-entrapped pores present in the AM fabricated components. In addition, the defect having a half-span width of 2 mm and crack length up to 4 mm were considered for the analysis.

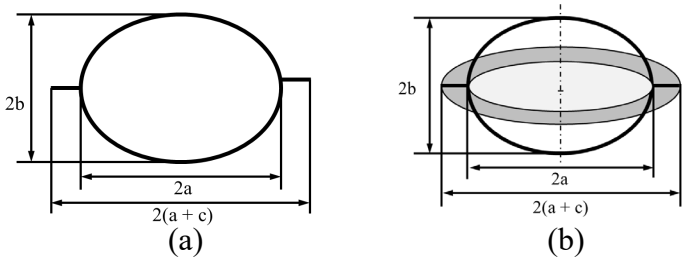

Fig. 1. Defect configurations considered in the FEA: (a) 2D internal and (b) 3D internal defect configurations.

The analysis was performed using the ABAQUS ™ software on the quarter and 1/8th portion of the 2D and 3D defect models respectively with symmetric boundary conditions applied. The 2D analysis was performed in plane strain conditions. These finite element models (FEM) were meshed and refined until the convergence in the SIF was attained (see **Fig. 2**). The finite element models were meshed using the quadratic brick elements (i.e., C3D20R elements) in the crack contour region and the tetrahedron elements (i.e., C3D10 elements) in the remaining portion of the model. In both 2D and 3D models, remote normal stress of 100 MPa was applied perpendicular to the crack plane. The SIF of the cracks was obtained using J-integrals for multiple

crack contours surrounding the crack tip and only the converged values were used for the analysis. Similar element types and methodology has been used by Courtin et al. [20] to obtain the SIF along the three-dimensional semi-elliptical crack front. To validate the results from FEA, the SIF of pure embedded cracks in infinite media in both 2D (straight crack) and 3D (penny-shaped crack) configurations are validated against analytical solutions [21][22].

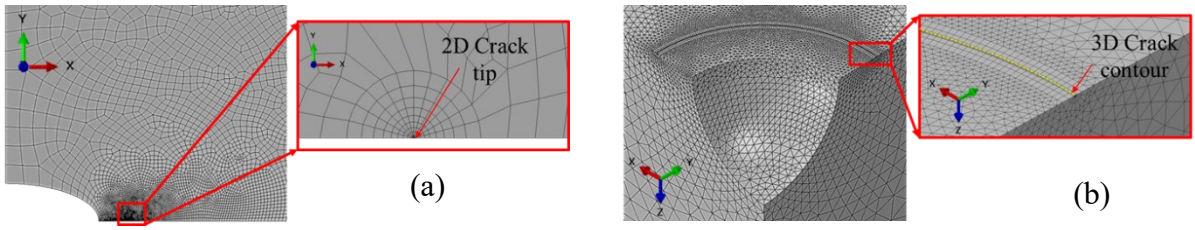

Fig. 2. The meshes for the FEA of (a) 2D internal and (b) 3D internal defect models with cracks.

Results and discussions

K_I for cracks of different lengths from defects of different shapes was obtained in both 2D and 3D configurations. In 2D models, the SIF was obtained at a single crack tip whereas, in 3D ones, it was obtained along the entire crack contour. In the case of 3D internal defects, the SIF along the entire crack contour was observed to be equal. The obtained SIF for both 2D and 3D configurations was plotted against the increasing crack length from the defect as seen in **Fig. 3**. The K_I was obtained for the defects with aspect ratios (b/a) of 0, 0.01, 0.2, 0.4, 0.6, 0.8, 1, and ∞. The pure crack configuration was assumed to have a b/a of 0 where the width of the crack is ignored. For the defect-free configuration, the effective aspect ratio is infinity.

The shape of the defect was observed to influence the SIF of the crack. As seen in **Fig. 3**, the defect having a lower aspect ratio (i.e., b/a) was observed to generate a higher SIF for small crack lengths. However, such influence of defect shape on K_I was only observed in the short crack length regime. The SIF calculated from 3D models was observed to be higher in comparison with the 2D models of the same defect shape and size. At a sufficient crack length, the effect of defect shape on SIF was observed to have been minimized and finally merge with the pure crack case (i.e., b/a = 0). In short crack length regimes, the defects such as lack of fusion (i.e., b/a ~0) were observed to generate higher K_I than a spherical pore (i.e., b/a ~1) of the equal effective defect sizes. Similar observations were made for both 2D and 3D configurations however, the values were slightly higher for the 3D configurations. In addition, the FEA SIF solutions for pure cracks in 2D (strain crack) and 3D (penny shaped crack) configurations were compared to analytical solutions [21][22]:

$$\text{2D: } K_I = \sigma\sqrt{\pi a}$$
$$\text{3D: } K_I = \frac{2}{\pi}\sigma\sqrt{\pi a} \quad (1)$$

where σ is the applied normal stress, and a is the half-span pure crack length. The FEA results were found to be within 0.1% accuracy from the analytical solutions.

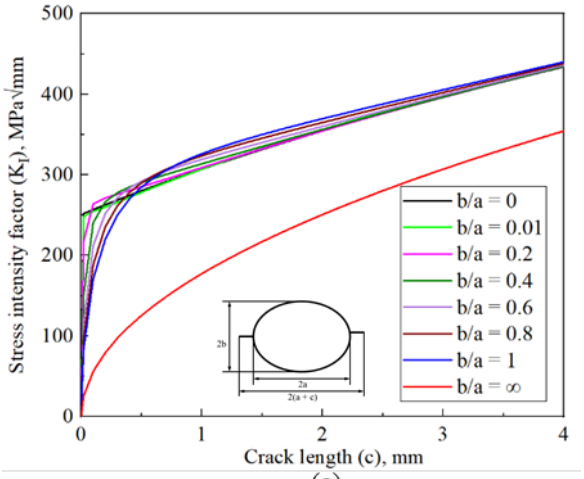

(a)

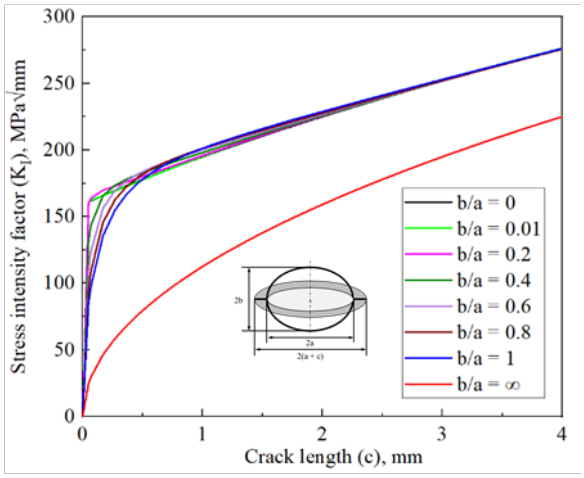

(b)

Fig. 3. Effect of defect shape on the Mode-I SIF of the crack originating from the (a) 2D and (b) 3D internal defect.

First, curve-fitting was performed on the data in **Fig. 3** to correlate the shape of the defect with K_I. As a result, **Eqs. 2** and **3** were generated to represent the K_I solution for 2D and 3D internal defects, respectively.

$$K_I = F\,\sigma\,\sqrt{\pi\,c} \tag{2}$$

$$K_I = 0.637\,F\,\sigma\,\sqrt{\pi\,c} \tag{3}$$

where F is the notch concentration factor, σ is the applied normal stress, and c is the crack length measured from the defect boundary. The notch concentration factor used in **Eqs. 2** and **3** were obtained using **Eq. 4** which correlated the shape of the defects with the K_I.

$$F = A_1 + \frac{A_2}{\sqrt{(a_{eff}-A_4)}} + \frac{A_3}{\sqrt[3]{(a_{eff}-A_4)}} \tag{4}$$

where a_{eff} is the effective defect size (i.e., a+c) and A_1, A_2, A_3, and A_4 are the parameters dependent on the shape of the defect. These parameters were obtained by fitting **Eqs. 5** and **6** for 2D and 3D

internal defects, respectively, to the data generated from FEA. In addition, the fitted parameters are listed in **Table 1**.

$$A_i = C_1^i + C_2^i \left(\frac{b}{a}\right) + C_3^i \left(\frac{b}{a}\right)^2 + C_4^i \left(\frac{b}{a}\right)^3 \quad (5)$$

$$A_j = C_1^j + C_2^j \left(\frac{b}{a}\right) + C_3^j \left(\frac{b}{a}\right)^2 + C_4^j \left(\frac{b}{a}\right)^3 \quad (6)$$

Table 1. Constants used for **Eqs. 6** and **7** for both 2D and 3D internal defects

2D internal defect				
i	C_1^i	C_2^i	C_3^i	C_4^i
1	1.1	0.338	-0.074	
2	2.115	2.083	0.224	
3	-1.48	-2.25	0.085	
4	1.99	-7.7	-0.4	0.017
3D internal defect				
j	C_1^j	C_2^j	C_3^j	C_4^j
1	1.11	0.2	0.134	-0.173
2	2.175	0.86	2.355	-1.79
3	-1.527	-1.06	-1.97	1.67
4	1.996	0.06	-0.513	0.19

Furthermore, the K_I for a defect with half-span width in the range of 10-100 μm was calculated utilizing the above results. In order to obtain the SIF for a different defect size, the units for both sizes as well as SIF should be consistent. Hence, the defect size was scaled by multiplying the horizontal axis of **Fig. 3** by a scaling factor and the vertical axis by a square root of the scaling factor. As a result, the SIF was obtained for defects with the half-span width of 10, 40, 70, and 100 μm as seen in **Fig. 4**. As expected, the SIF of the cracks originating from the defects with different sizes increases with the increase in the crack length. The SIF also increases with the increasing defect size. Interestingly, the increasing trend of the SIF with the crack length varied with the shape of the defect (i.e., b/a). It was observed to increase gradually for the defects with a higher aspect ratio (i.e., b/a=1) and increase sharply for lower aspect ratio defects (i.e., b/a=0) (see **Fig. 4**(a) and (b)). The trend was similar in the case of both 2D and 3D models.

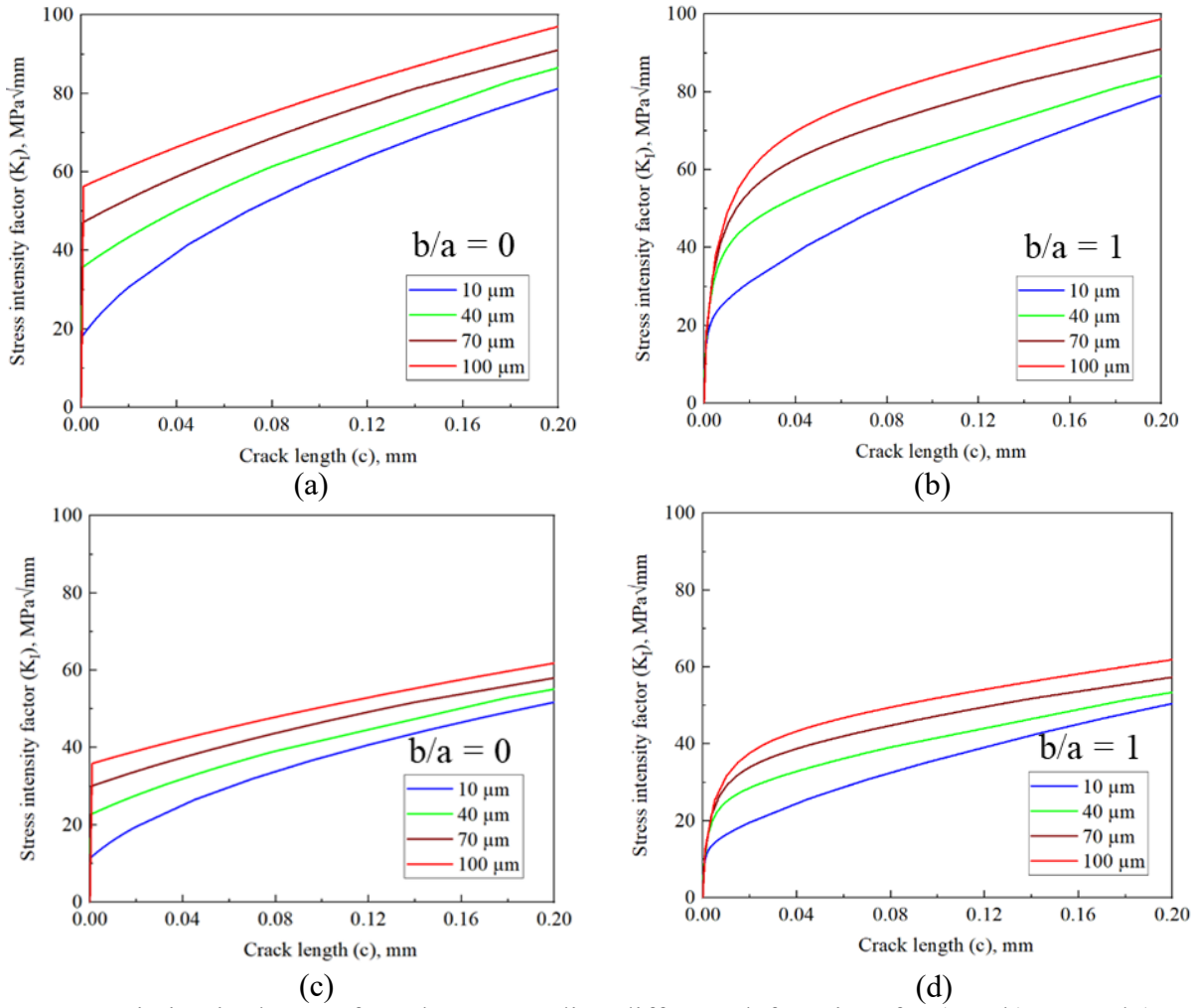

Fig. 4. Variation in the K_I of cracks surrounding different defect sizes for (a & b) 2D and (c & d) 3D internal defect configurations having aspect ratio b/a = 0 and b/a = 1, respectively.

Conclusions

In this study, the effect of defect shape, as well as size on Mode-I stress intensity factor of the crack originating from the internal defects, was investigated. The following are the major conclusions derived from the study.

1. The defects having a lower aspect ratio (i.e., the ratio of depth and width) generated a higher Mode-I stress intensity factor (K_I) for a short crack length.
2. The effect of defect shape on the stress intensity factor of crack exists only in the short crack length regime.

Acknowledgment

This material is based upon work partially supported by the National Institute of Standards and Technology (NIST) under grant No. 70NANB19H170.

References

[1] N. Shamsaei, A. Yadollahi, L. Bian, S.M. Thompson, An overview of Direct Laser Deposition for additive manufacturing; Part II: Mechanical behavior, process parameter optimization and control, Addit. Manuf. 8 (2015) 12–35. https://doi.org/10.1016/j.addma.2015.07.002.

[2] A. Yadollahi, N. Shamsaei, Additive manufacturing of fatigue resistant materials: Challenges and opportunities, Int. J. Fatigue. 98 (2017) 14–31. https://doi.org/10.1016/j.ijfatigue.2017.01.001.

[3] I. Serrano-Munoz, J.Y. Buffiere, R. Mokso, C. Verdu, Y. Nadot, Location, location &size: Defects close to surfaces dominate fatigue crack initiation, Sci. Rep. 7 (2017) 1–9. https://doi.org/10.1038/srep45239.

[4] T. DebRoy, H.L. Wei, J.S. Zuback, T. Mukherjee, J.W. Elmer, J.O. Milewski, A.M. Beese, A. Wilson-Heid, A. De, W. Zhang, Additive manufacturing of metallic components – Process, structure and properties, Prog. Mater. Sci. 92 (2018) 112–224. https://doi.org/10.1016/j.pmatsci.2017.10.001.

[5] R.I. Stephens, A. Fatemi, R.R. Stephens, H.O. Fuchs, Metal Fatigue in Engineering, 2nd ed., John Wiley & Sons, 2000.

[6] A. Yadollahi, N. Shamsaei, Additive manufacturing of fatigue resistant materials: Challenges and opportunities, Int. J. Fatigue. 98 (2017) 14–31. https://doi.org/10.1016/j.ijfatigue.2017.01.001.

[7] G.R. Halford, Fatigue and Durability of Structural Materials, ASM International, 2006.

[8] X. Ma, Z. Duan, H. Shi, R. Murai, E. Yanagisawa, Fatigue and Fracture Behavior of Nickel-Based Superalloy Inconel 718 up to the Very High Cycle Regime, J. Zhejiang Univ. Sci. A. 11 (2010) 727–737. https://doi.org/10.1631/jzus.A1000171.

[9] A.J. Sterling, B. Torries, N. Shamsaei, S.M. Thompson, D.W. Seely, Fatigue behavior and failure mechanisms of direct laser deposited Ti-6Al-4V, Mater. Sci. Eng. A. 655 (2016) 100–112. https://doi.org/10.1016/j.msea.2015.12.026.

[10] S. Lee, J.W. Pegues, N. Shamsaei, Fatigue behavior and modeling for additive manufactured 304L stainless steel: The effect of surface roughness, Int. J. Fatigue. 141 (2020) 105856. https://doi.org/10.1016/j.ijfatigue.2020.105856.

[11] S. Romano, L. Patriarca, S. Foletti, S. Beretta, LCF behaviour and a comprehensive life prediction model for AlSi10Mg obtained by SLM, Int. J. Fatigue. 117 (2018) 47–62. https://doi.org/10.1016/j.ijfatigue.2018.07.030.

[12] P.D. Nezhadfar, E. Burford, K. Anderson-Wedge, B. Zhang, S. Shao, S.R. Daniewicz, N. Shamsaei, Fatigue crack growth behavior of additively manufactured 17-4 PH stainless steel: Effects of build orientation and microstructure, Int. J. Fatigue. 123 (2019) 168–179. https://doi.org/10.1016/j.ijfatigue.2019.02.015.

[13] X. Zhang, F. Martina, A.K. Syed, X. Wang, J. Ding, S.W. Williams, Fatigue Crack Growth in Additive Manufactured Titanium: Residual stress control and life evaluation method development, 29 Th ICAF Symp. (2017) 7–9.
[14] M.H. El Haddad, K.N. Smith, T.H. Topper, Fatigue crack propagation of short cracks, J. Eng. Mater. Technol. Trans. ASME. 101 (1979) 42–46. https://doi.org/10.1115/1.3443647.
[15] M.H. El Haddad, T.H. Topper, T.N. Topper, Fatigue life predictions of smooth and notched specimens based on fracture mechanics, J. Eng. Mater. Technol. Trans. ASME. 103 (1981) 91–96. https://doi.org/10.1115/1.3224996.
[16] M.H. El Haddad, T.H. Topper, K.N. Smith, Prediction of non propagating cracks, Eng. Fract. Mech. 11 (1979) 573–584. https://doi.org/10.1016/0013-7944(79)90081-X.
[17] M. Yukitaka, E. Masahiro, Quantitative evaluation of fatigue strength of metals containing various small defects or cracks, Eng. Fract. Mech. 17 (1983) 1–15. https://doi.org/10.1016/0013-7944(83)90018-8.
[18] J.C. Sobotka, M.P. Enright, R.C. McClung, Application of critical distances to fatigue at pores, Fatigue Fract. Eng. Mater. Struct. 42 (2019) 1646–1661. https://doi.org/10.1111/ffe.13004.
[19] G.R.I. Hiroshi Tada, Paul C. Paris, Stress Analysis of Cracks Handbook Excerpts, (2000) 40–47.
[20] S. Courtin, C. Gardin, G. Bézine, H.B.H. Hamouda, Advantages of the J-integral approach for calculating stress intensity factors when using the commercial finite element software ABAQUS, Eng. Fract. Mech. 72 (2005) 2174–2185. https://doi.org/10.1016/j.engfracmech.2005.02.003.
[21] D. Broek, J.R. Rice, Elementary Engineering Fracture Mechanics, J. Appl. Mech. 42 (1975) 751–752. https://doi.org/10.1115/1.3423697.
[22] T.L. Anderson, Fracture mechanics: fundamentals and applications, CRC Press, 2005.